

Microstructural and magnetic evolution upon annealing of giant magnetoresistance melt-spun Co-Cu granular alloys

A. García Prieto,^{1,*} M. L. Fdez-Gubieda,¹ C. Meneghini,^{2,3} A. García-Arribas,¹ and S. Mobilio^{3,4}

¹*Departamento de Electricidad y Electrónica. Universidad del País Vasco, Apartado 644, 48080 Bilbao, Spain*

²*Istituto Nazionale di Fisica della Materia (INFN), c/o ESRF GILDA CRG, Boîte Postal 220, F-38043 Grenoble, France*

³*Dipartimento di Fisica "E. Amaldi," Università di Roma Tre, Via della Vasca Navale 84, I-00146 Roma, Italy*

⁴*Laboratori Nazionali di Frascati (INFN), P.O. Box 13, I-00044 Frascati, Italy*

(Received 5 November 2002; revised manuscript received 25 March 2003; published 13 June 2003)

This paper reports a thorough microstructural and magnetic analysis performed on as-quenched and annealed melt-spun $\text{Co}_x\text{Cu}_{100-x}$ granular alloys presenting giant magnetoresistance. The use of three different techniques has been necessary to follow the evolution of the Co atoms with the thermal treatment. X-ray diffraction (XRD) detects the fraction of the Co atoms which are arranged in nanometric clusters. From the analysis of the hysteresis loops we have identified three different Co arrangements, each one with a different magnetic response: Co superparamagnetic nanoclusters, a Co-rich ferromagnetic phase, previously detected by XRD, and Co atoms diluted into the Cu matrix with no magnetic contribution. Finally, by means of the extended x-ray absorption fine structure spectroscopic technique performed on the Co K edge, we have analyzed the local configuration of the Co atoms, in particular, at the interfaces between the magnetic nanoclusters and the Cu matrix. Using the information gathered with these techniques, the microstructural evolution has been correlated to the giant magnetoresistance response of the CoCu system.

DOI: 10.1103/PhysRevB.67.224415

PACS number(s): 61.46.+w, 61.10.Ht, 61.10.-i, 75.70.-i

I. INTRODUCTION

The giant magnetoresistance (GMR) phenomenon is a huge decrease of the electrical resistance when a magnetic field is applied. This phenomenon was first discovered in samples composed of alternating layers of a magnetic and nonmagnetic layers.¹ Afterwards, the GMR was also observed in granular samples^{2,3} composed of clusters of a magnetic element embedded in a nonmagnetic metallic matrix. The GMR effect in granular systems is attributed to the same physical mechanisms as in multilayers, that is, spin-dependent scattering of the conducting electrons at the magnetic clusters. Although the microscopic origin of the GMR is still unresolved, it is generally accepted that the spin scattering occurs predominantly at the interfaces of the magnetic clusters and the metallic matrix.⁴⁻⁷ Thus, small magnetic clusters enhance the GMR because the smallest their size, the highest the number of atoms at the interface. However, there are other structural properties of the granular samples that influence on their GMR response; in fact, the GMR response of the granular samples is generally attributed to a competition among the surface-to-volume ratio, concentration, and/or size-distribution of the magnetic particles, their magnetic state and the magnetic interactions among them.^{4,9,6,7,10,8,11} The important role of the structure of the interfaces between the magnetic granules and the metallic matrix has been also underlined.¹²⁻¹⁴

Granular alloys are usually composed of two immiscible elements, one magnetic and the other a metallic nonmagnetic one, such as Ag-Co, Cu-Co, Ag-Fe, or Cu-Ni.¹⁵ A metastable solid solution of both elements is obtained with the use of ultrarapid techniques such as electrodeposition, sputtering, laser ablation, or melt spinning.^{16,17} The microstructure of these metastable alloys is easily modifiable by suitable thermal treatments: the supplied thermal energy is spent in obtaining a more stable state by the precipitation of both ele-

ments that compose the alloys. Therefore, granules of the minority element grow embedded into the matrix of the majority one.

In this work, we have studied $\text{Co}_x\text{Cu}_{100-x}$ ($x = 5, 10, 15, 20$) melt-spun granular alloys in the as-quenched state and annealed at increasing temperatures between 400 and 650 °C. As reported elsewhere,^{14,18-21} the evolution of the GMR response of the CoCu granular alloys with the annealing temperature is independent of the sample composition (x), that is, it increases slowly from the as-quenched state to the annealed at 450 °C, where it reaches the maximum value, and at 500 °C it drops abruptly and continues decreasing until the end of the thermal treatment. Although the CoCu granular system has been extensively studied in recent years, there are no conclusive results about its real microstructure, mostly due to the experimental difficulty of resolving small structures out of a matrix when the elements involved have very close atomic numbers, as for Co and Cu. The relevant information gathered about these systems comes mainly from macroscopic evidence, such as magnetic and transport properties from which the microscopic information available is deduced using more or less accurate models. In this work, we report a thorough microstructural study that has allowed us to follow in detail the changes that the thermal annealing causes in the microstructure of the samples, in particular in the distribution of the Co atoms. This way, we have completed a previous work¹⁴ where we presented preliminary results and strengthened the important role of the interface in the GMR response of the samples.

The melt-spinning method produces inhomogeneous samples: in the as-quenched state the Co atoms are mainly diluted into the Cu matrix and/or forming nanoclusters with a superparamagnetic response. The thermal treatment induces the segregation of the Co atoms and the diluted part dimin-

ishes on behalf of the superparamagnetic and/or ferromagnetic phases. By means of three complementary techniques we have been able to study the microstructural evolution of the samples with the annealing. First of all, we have used the x-ray diffraction (XRD) technique. This technique detects crystalline phases having long-range structural order (on a scale no smaller than some ten nm). Therefore, it is able to probe mainly the large Co clusters which are responsible for the ferromagnetic behavior but will not detect the presence of Co nanoclusters and/or the Co atoms diluted in the Cu matrix. Secondly, the magnetic study through the analysis of the hysteresis loops of the samples has provided us very useful microstructural information concerning the Co containing phases. From the different magnetic responses of each Co arrangement we have been able to complement the previous information of the XRD analysis about the ferromagnetic phase and to reveal and quantify the percentage of Co not detectable by XRD because it is forming superparamagnetic Co nanoclusters, and/or is diluted into the Cu matrix. These Co nanoclusters are responsible of the GMR behavior. Finally, the extended x-ray absorption fine structure (EXAFS) technique is a local probe (on a scale of a few Å), very sensitive to the local structure around the absorber atom. In this case, we have exploited the EXAFS technique for studying the surroundings of the Co atoms as a function of the thermal treatment and, in particular, for probing the evolution the Co-Co interatomic distances and the structural disorder around the Co atoms. This concise study has allowed us to gain precise knowledge of the microstructure of the samples at each stage of the thermal treatment and to certify the close correlation between the microstructure and the GMR response in granular alloys, in particular the important role of the Co-nanoclusters interfaces.

The paper is distributed as follows. In Sec. II we present the experimental techniques, in Sec. III the data analysis and results, and in Sec. IV the discussion. Finally, we briefly outline the the main conclusions in Sec. V.

II. EXPERIMENTAL TECHNIQUES

We have studied a series of $\text{Co}_x\text{Cu}_{100-x}$ ($x=5,10,15,20$) samples prepared by rapid quenching in the form of long ribbons of about 30 μm thick. 1-cm long pieces of each sample were thermal annealed at these annealing temperatures $T_{\text{ann}}=400,450,500,550,600,650$ °C during 30 min in an Ar controlled atmosphere furnace in order to avoid oxidation. For each composition, the very same piece of sample was used for all the experiments.

The magnetoresistance (MR), defined as the change of the electrical resistance R under an applied magnetic field $\mu_0 H$

$$\text{MR}(\%) = \frac{R(\mu_0 H) - R(\mu_0 H = 0)}{R(\mu_0 H = 0)} \times 100, \quad (1)$$

has been measured at 10 K using the conventional four points configuration. The measuring loop was $0\text{ T} \rightarrow 7\text{ T} \rightarrow -7\text{ T} \rightarrow 0\text{ T}$. The hysteresis loops were recorded at 300 K with a magnetic field up to 7 T. Both measurements were performed in a SQUID magnetometer.

TABLE I. Values of the GMR at 7 T and 10 K.

	aq	400 °C	450 °C	500 °C	550 °C	600 °C	650 °C
$x=5$	4.2	12.1	21.4	14.3	6.1	3.3	–
$x=10$	12.1	25.2	27.1	22.4	13.5	4.7	–
$x=15$	11.6	31.9	30.9	21.5	9.4	3.0	–
$x=20$	16.2	25.2	26.6	16.9	6.4	2.4	–

X-ray diffraction and absorption experiments were carried on in the GILDA beamline²² at the European Synchrotron Radiation Facility (ESRF) in Grenoble (France). High-resolution XRD patterns were obtained using a two-circle diffractometer equipped with a Ge(111) crystal analyzer on the diffracted beam. The instrumental line broadening is full width at half maximum (FWHM) $2\theta < 0.01^\circ$. The XRD patterns were collected at room temperature using a wavelength of 0.9535 Å. For $x=5,10$, and 20 samples, measurements were performed for all annealing stages, in the angular range $22 < 2\theta < 88^\circ$. Additional spectra with better statistics were collected in the region around the (111) Bragg peaks ($22 < 2\theta < 30$). X-ray spectra for $x=15$ were also taken for the as-quenched state and 400 °C annealing. For all the samples, as-quenched and annealed, XRD patterns were also collected using an angle dispersed setup based on a 2D imaging plate detector.²² The wavelength was 1.0334 Å and the instrumental resolution 0.06–0.07° in 2θ . Notice that even if the area detectors cannot reach the angular resolution and the absolute accuracy on lattice parameters available on a high resolution diffractometer, the 2D geometry offers several advantages and gives useful complementary information. In fact, the very high count statistics allows one to detect and perform a reliably characterization also of those phases having relatively weak signal. Moreover, the possibility to integrate the diffraction pattern over a large portion of the Debye rings allows one to reduce the effect of privileged orientation on the sample and is mandatory for an accurate and reliable analysis of peak area and shape.

Co K-edge EXAFS spectra were collected at 77 K in $x=5,15$, and 20 as-quenched and annealed samples in transmission geometry. On the other hand, EXAFS measurements of $x=10$ samples were collected at room temperature in station 7.1 at the Daresbury Synchrotron Radiation Source (SRS), U.K. The monochromator used in the measurements was a double monocrystal of Si oriented in the (111) direction.

III. DATA ANALYSIS AND RESULTS

A. Giant magnetoresistance (GMR)

The measurement of the MR at 10 K and up to a magnetic field as high as 7 T allows one to reach the saturation value of the MR for all the annealed samples. Table I displays the values of the GMR at 7 T as a function of T_{ann} for each composition x . The evolution of the modulus of the MR with the annealing temperature is similar for the four compositions studied: it increases up to 450 °C and starts to decrease at 500 °C. The maximum value of the GMR (32%) was found for the $x=15$ alloy.

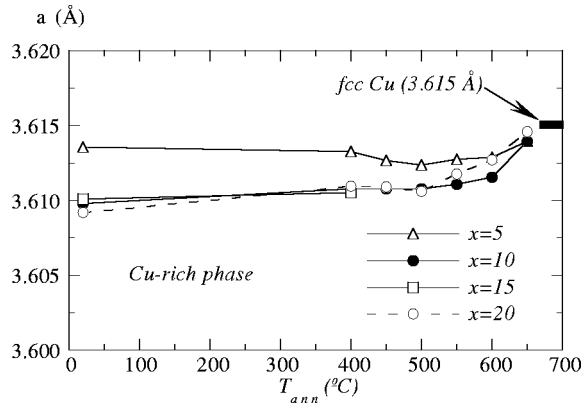


FIG. 1. Evolution of the Cu-rich fcc phase lattice parameters obtained from the analysis of the room temperature high-resolution XRD patterns.

B. X-ray diffraction (XRD)

High-resolution x-ray diffraction patterns of samples $x = 5$ display one set of peaks that corresponds to a Cu-rich fcc phase. On the other hand, the diffractograms of samples $x = 10, 15$, and 20 reveal the existence of two fcc phases: one corresponds to a Cu-rich phase and the other to a Co-rich phase. It is important to note that both phases appear even in the as-quenched state.

The high resolution XRD and the XRD patterns collected using the angle dispersed setup were used for giving complementary information in the following way: from the analysis of the high-resolution patterns we have been able to extract the evolution of the lattice parameters as a function of thermal treatment and composition with very high accuracy. Analyzing the patterns obtained using the angle dispersed setup we have been able to carefully estimate the areas of the peaks and thus the relative percentage of each phase in the samples. Diffraction patterns (high-resolution and 2D-angle dispersed) were thoroughly analyzed by means of the Rietveld profile refinement method as implemented in the GSAS software,²³ and the XRD peak shape was modeled with a pseudo-Voigt function.

Line-shape analysis on the XRD patterns indicates that grain size in the Cu-rich phase is about 90–100 nm, whereas the Co-rich phase, in $x = 10, 15$, and 20 samples, is composed of crystallites that grow in size with the annealing temperature from about 20–30 to 90–100 nm. This is an important finding from the point of view of the magnetic analysis, because a 20–30 nm size Co granule is expected to display a ferromagnetic (FM) response.²⁴ For this reason, in the following, and in order to not confuse the different arrangements of the Co atoms, we will call this fcc phase the *Co-rich FM phase*.

The evolution of the lattice parameter as a function of the annealing temperature is presented in Fig. 1 for the Cu-rich phase and in Fig. 2(a) for the Co-rich FM phase. Finally, by measuring the Co and Cu peaks area (A_{Co} , A_{Cu}) on the 2D-angle dispersed diffractograms, we have estimated the percentage of this Co-rich phase ($X_{Co}\%$) from the proportionality between both parameters

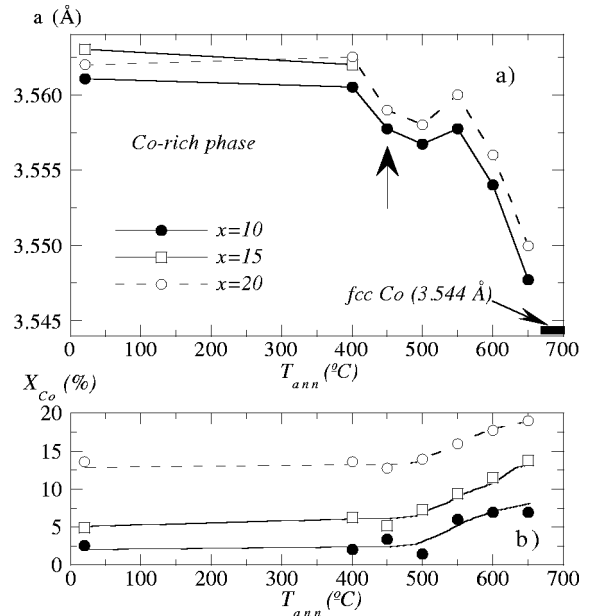


FIG. 2. (a) Evolution of the lattice parameters obtained from the analysis of the room temperature high-resolution XRD patterns for the Co-rich fcc phase. Note that the y-axis scale is the same as in Fig. 1. The arrow marks the point where the MR is maximum. (b) Percentage of Co-rich FM phase ($X_{Co}\%$) as calculated from the peaks area of the 2D-angle dispersed spectra (data of Table II). The continuous line is a guide for the eye.

$$\frac{A_{Cu}}{A_{Co}} \propto \frac{X_{Cu}}{X_{Co}} \quad (2)$$

and the condition $X_{Cu} + X_{Co} = 100$. If Cu and Co atoms were completely separated in two different phases we would have $X_{Cu}/X_{Co} = (100 - x)/x$. The results of these calculi are presented in Table II. The fact that $X_{Co}\% < x$ in all the samples studied, even those annealed at 650 °C, means that the rest of the Co atoms are diluted into the Cu matrix or/and arranged in clusters too small to be detected by this technique. We must note that even if the evaluation of Co-rich phase peak area is affected by larger uncertainty, owing to the relative weakness of its contribution with respect to that of the Cu-rich phase, the results of these calculi ($X_{Co}\%$) show a trend as a function of thermal treatment consistently reproduced for all the compositions, that is, the percentage of Co is almost unchanged up to 550 °C and for $T_{ann} \geq 550$ °C it increases approaching the total amount of Co in the samples (x), as observed in Fig. 2 in which we have plotted the data of Table II in order to remark this feature. In the as-quenched state $X_{Co}\%$ is a minority part of all the Co for $x = 10$ and 15 samples (2.6 and 4.9 %, respectively) and a higher amount is found for $x = 20$ samples (13.6 %). But at $T_{ann} = 650$ °C the majority of the Co in the samples (7.3, 14, and 19 % for $x = 10, 15$, and 20 , respectively) is forming this ferromagnetic phase of 90–100 nm size. These results will be taken into account when analyzing the hysteresis loops of the samples.

C. Hysteresis loops

The evolution of the hysteresis loops with T_{ann} is similar for the four concentrations (x) studied: the hysteresis loops

TABLE II. Values of the percentage of Co in the Co-rich phase ($X_{\text{Co}}\%$) obtained from the peaks area in the DRX 2D-angle dispersed spectra [these data are also displayed in Fig. 2(b)] and percentages of each magnetic phase as calculated in the magnetic analysis [Eq. (10)].

		aq	400 °C	450 °C	500 °C	550 °C	600 °C	650 °C
$x = 5$	$X_{\text{Co}}\%$	0	0	0	0	0	0	0
	% FM	0	0	0	0	0	–	–
	% SPM	2.55(5)	4.05(5)	4.85(5)	4.35(5)	4.25(5)	–	–
	% dil.	2.45(5)	0.95(5)	0.15(5)	0.65(5)	0.75(5)	–	–
$x = 10$	$X_{\text{Co}}\%$	2.6(6)	2.1(4)	3.4(7)	1.5(5)	6(1)	7(1)	7(1)
	% FM	1.9(2)	1.9(2)	1.5(2)	1.4(1)	6.3(1)	–	9.0(5)
	% SPM	6.1(2)	7.4(2)	7.2(2)	7.6(1)	2.5(2)	–	0
	% dil.	2.0(3)	0.7(3)	1.3(3)	1.0(2)	1.2(2)	–	1.0(5)
$x = 15$	$X_{\text{Co}}\%$	4.9(7)	6.3(6)	5.2(4)	7.3(6)	9.4(3)	11.5(7)	13.8(7)
	% FM	2(1)	5.5(3)	4.5(3)	4.8(3)	8.5(6)	–	14.2(4)
	% SPM	6(1)	6.9(3)	9.7(3)	8.8(3)	4.8(6)	–	0
	% dil.	7(1)	2.6(4)	0.8(4)	1.4(4)	1.7(9)	–	0.7(4)
$x = 20$	$X_{\text{Co}}\%$	13.6(8)	13.6(8)	12.8(6)	14(6)	16.0(4)	17.8(6)	19.0(8)

of the as-quenched and annealed at $T_{\text{ann}} < 550$ °C samples are not saturated even at a magnetic field as high as 7 T and present small coercivities (between 60 and 230 Oe) and remanence, while for $T_{\text{ann}} \geq 550$ °C well-saturated hysteresis loops are obtained. As an example, we display in Fig. 3 the evolution of the hysteresis loops with the annealing temperature (T_{ann}) for $x = 15$ as-quenched and annealed samples measured at 300 K. The nonsaturating behavior of the hysteresis loops is due to the presence of Co nanoclusters forming a superparamagnetic (SPM) phase. On the other hand, the coercivity and remanence of the loops have two different origins: first of all, in $x = 5$ samples, where no Co-rich FM phase was detected by XRD even at the last stages of the annealing, we propose that they appear due to dipolar interactions between the SPM nanoclusters. Second, in $x = 10, 15$, and 20 samples, we attribute the coercivity and remanence of the loops to the several-ten-nm-sized fcc Co-rich ferromagnetic phase previously observed in the XRD analysis. As deduced from Table II, $X_{\text{Co}}\%$ increases with the annealing temperature and approaches the totality of the Co in the samples (x), what explains that at higher annealing temperatures ($T_{\text{ann}} \geq 550$ °C) the hysteresis loops are well-saturated and thus display a dominant FM behavior.

The SPM contribution to the total magnetization is described by the Langevin law²⁵

$$M^{\text{SPM}} = M_s^{\text{SPM}} \mathcal{L}(a), \quad \text{where} \quad \mathcal{L}(a) = \coth a - \frac{1}{a}, \quad (3)$$

where M_s^{SPM} is the saturation magnetization of the SPM phase and $a = \mu \mu_0 H / k_B T$. μ is the magnetic moment of the Co nanoclusters given by $\mu = M_s^{\text{fcc Co}} (\pi D^3 / 6)$, where $\pi D^3 / 6$ is the volume of the clusters, assumed spheres with diameter D , and $M_s^{\text{fcc Co}} = 164.8$ Am²/kg is the saturation magnetization of the bulk fcc Co. In order to take into account the

different sizes of the SPM Co clusters in the sample we have introduced a log-normal size distribution function $f(D)$, which is defined as²⁶

$$f(D) = \frac{1}{\sqrt{2\pi} D \beta} \exp\left(-\frac{\ln^2(D/\alpha)}{2\beta^2}\right), \quad (4)$$

and depends on two parameters, α and β . The mean particle diameter (\bar{D}) and the standard deviation (σ) are given by

$$\bar{D} = \alpha e^{\beta^2/2}, \quad \sigma^2 = \bar{D}^2 \left(\frac{\bar{D}^2}{\alpha^2} - 1 \right). \quad (5)$$

The SPM contribution to the total magnetization of an array of Co nanoclusters with a size distribution function given by Eq. 4 is described by

$$M^{\text{SPM}} = M_s^{\text{SPM}} \int_0^\infty f(D) \mathcal{L}(a) dD. \quad (6)$$

In a SPM system with dipolar interactions among the nanoclusters, Allia *et al.*²⁷ suggest that the anhysteretic curve, given by

$$\Sigma = \frac{1}{2} (M^+ + M^-), \quad (7)$$

where M^+ and M^- are the magnetization of the positive and negative branches, respectively, must follow the Langevin law. In our case, we have applied this model to the $x = 5$ samples, and therefore fitted the Langevin equation [Eq. (6)] to the calculated anhysteretic loops of the as-quenched and annealed $x = 5$ samples.

On the other hand, for $x = 10, 15$, and 20 samples, where the FM contribution to the total magnetization comes from

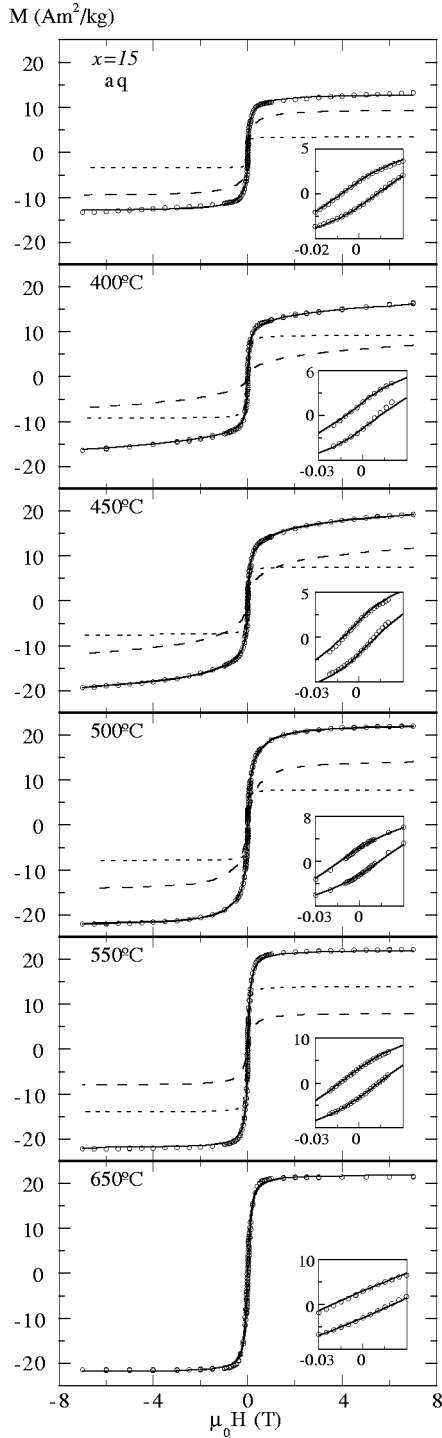


FIG. 3. Hysteresis loops of samples $x=15$ as-quenched and annealed at $T_{\text{ann}}=400,450,500,550,$ and 650 °C measured at 300 K. The continuous line is the fitting of the samples with Eq. (9), the SPM (---) and FM (···) contributions to the total magnetization are also plotted. A detail of the fits at low magnetic fields is shown in the insets.

the Co-rich FM phase previously observed by XRD, we have implemented this FM contribution to the total magnetization by the following *ad hoc* equation suggested by Stearns *et al.*:²⁸

TABLE III. Values of the SPM phase parameters obtained from the fitting of the hysteresis loops. M_s^{SPM} is in Am^2/kg and \bar{D} and σ in nm.

	aq	400°C	450°C	500°C	550°C	650°C
$x=5$						
M_s^{SPM}	4.21(1)	6.66(8)	8.04(8)	7.18(1)	7.040(5)	–
\bar{D}	2.72(1)	1.68(2)	1.97(3)	2.71(1)	4.34(1)	–
σ	0.99(1)	1.14(2)	0.96(3)	0.87(1)	0.84(1)	–
$x=10$						
M_s^{SPM}	10.1(3)	12.2(3)	11.81(3)	12.5(1)	4.2(4)	0
\bar{D}	2.51(9)	2.52(6)	2.71(1)	2.96(1)	5.1(3)	–
σ	1.2(1)	1.20(7)	0.60(2)	0.87(2)	1.3(3)	–
$x=15$						
M_s^{SPM}	10(2)	11.3(5)	16.0(4)	14.5(5)	8(1)	0
\bar{D}	4.5(5)	1.2(3)	2.4(2)	3.31(7)	3.6(2)	–
σ	2.1(5)	2.2(6)	2.2(3)	0.94(7)	0.4(2)	–

$$M^{\text{FM}} = \frac{2M_s^{\text{FM}}}{\pi} \arctan \left[\frac{H \pm H_c}{H_c} \tan \left(\frac{\pi M_r}{2M_s^{\text{FM}}} \right) \right]. \quad (8)$$

In this expression, M_r is the remanent magnetization, M_s^{FM} is the saturation magnetization of the ferromagnetic phase, and H_c is the coercive field.

Thus, the theoretical expression of the total magnetization for $x=10,15,$ and 20 samples is

$$M = M^{\text{SPM}} + M^{\text{FM}} = M_s^{\text{SPM}} \int_0^\infty f(D) \mathcal{L}(a) dD + \frac{2M_s^{\text{FM}}}{\pi} \arctan \left[\frac{H \pm H_c}{H_c} \tan \left(\frac{\pi M_r}{2M_s^{\text{FM}}} \right) \right]. \quad (9)$$

The fitting of expression (9) to the experimental data has been implemented using the PROFIT package.²⁹ Six parameters have been fitted: $\alpha, \beta, M_s^{\text{FM}}, M_s^{\text{SPM}}$ and H_c . The remanent magnetization (M_r) has been fixed to the experimental value.

The results of the fitting for the SPM phase are displayed in Table III, and the corresponding to the FM phase, for $x=10,15,$ in Table IV. The fitted hysteresis loops of $x=15$ as-quenched and annealed at 400, 450, 500, 550, and 650 °C samples with the corresponding SPM and FM contributions are displayed in Fig. 3.

From the saturation magnetization of both magnetic phases given in Tables III and IV we have estimated quanti-

TABLE IV. Values of the FM phase parameters obtained from the fitting with Eq. (8) of the hysteresis loops of $x=10,15$ samples. M_s^{FM} is in Am^2/kg and H_c in Oe.

	aq	400°C	450°C	500°C	550°C	650°C
$x=10$						
M_s^{FM}	3.2(4)	3.1(4)	2.4(3)	2.39(4)	10.31(3)	14.85(9)
H_c	240(40)	250(30)	190(10)	350(30)	120(10)	123(3)
$x=15$						
M_s^{FM}	4(2)	9.2(6)	7.5(4)	7.8(5)	14(1)	23.5(1)
H_c	150(70)	150(10)	170(10)	172(8)	150(6)	160(20)

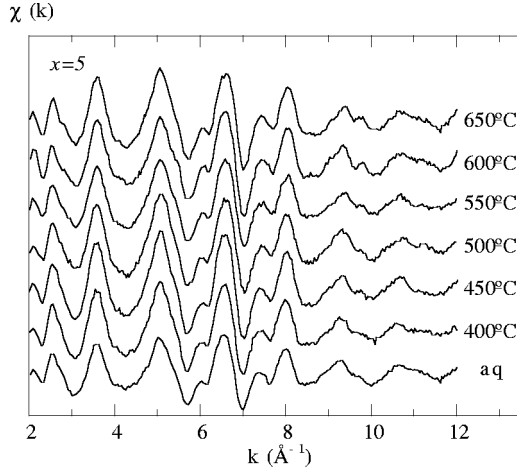


FIG. 4. EXAFS signals of the as-quenched and annealed $x=5$ samples collected at 77 K.

tatively the percentage of Co in each magnetic phase as the ratio of the corresponding saturation magnetization (SPM or FM) and the saturation magnetization of bulk fcc Co:

$$\% \text{ SPM(FM)} = \frac{M_s^{\text{SPM(FM)}}}{M_s^{\text{fcc Co}}} \times 100, \quad (10)$$

that is, we have considered that if all the Co in the sample (x) contributed magnetically, the total saturation magnetization of the sample would be that of the bulk fcc Co. The remaining percentage $[100 - (\% \text{ SPM} + \% \text{ FM})]$ represents the amount of Co atoms that do not contribute magnetically because are diluted into the Cu matrix. The results of these calculi are presented in Table II.

D. Extended x-ray absorption fine structure (EXAFS)

The structural EXAFS signals were extracted from absorption spectra using standard procedures for background subtraction and data normalization.³⁰ Systematical errors were minimized using the same procedure for all the data sets. The fine structure extended from 20 to 700 eV was first normalized to the jump of the K -absorption edge, then fitted using a cubic spline curve to remove the low frequency background oscillation and converted to photon-electron wave vector k space. The EXAFS signals $\chi(k)$ obtained for the Co K edge are displayed in Fig. 4 for the as-quenched and annealed $x=5$ samples. At a glance, no changes are observed with the thermal treatment due to the fact that Co and Cu have very similar backscattering properties. Afterwards, the range $2 < k < 12 \text{ \AA}^{-1}$ of the EXAFS signals were Fourier transformed to radial coordinates R in order to gain direct information about the structure around the Co sites. From the Fourier transforms some qualitative information can be obtained. It is noticeable that the amplitude of the first peak of the Fourier transform displays the same evolution with T_{ann} regardless of x : it grows until 450 °C, afterwards it decreases and then it increases again above 550 °C.

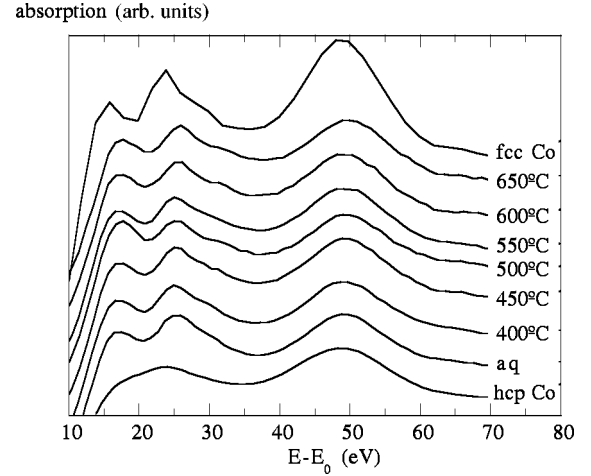


FIG. 5. XANES spectra of the Co K edge of the $x=15$ samples, fcc Co K edge, and hcp Co K edge. The similarity of the XANES spectra of the CoCu samples to that of the fcc Co demonstrates that the Co crystallizes in fcc structure in the CoCu granular samples.

Quantitative information about the local structure around the Co atoms and its evolution with the annealing temperature was obtained by fitting the filtered EXAFS data to the expression³¹

$$k\chi(k) = \sum_j S_0^2 N_j f_j(k, \pi) \frac{e^{-2\sigma_j^2 k^2} e^{-2\Gamma_j/k}}{R_j^2} \sin[2kR_j + \phi_j(k, \pi)]. \quad (11)$$

The sum expands over all the species of backscattering atoms at the same distance R_j of the central atom with variance σ_j^2 (Debye-Waller factor) around the absorber, and N_j is the number of such atoms. The scale factor S_0^2 is related to the many body effects and $e^{-2\Gamma_j/k}$ is a mean free path term that takes into account the inelastic losses of the photoelectron. $f_j(k, \pi)$ is the magnitude of the effective curved-wave backscattering amplitude for the j th type of atoms and $\phi_j(k, \pi) = [2\delta(k) - \pi] + \Phi_j(k)$, where the first and second terms represent the modification in the phase shift of the ejected photoelectron wave function by the potential of the central absorbing and backscattering atoms, respectively. In our case, the central atom is Co and two types of scattering atoms must be taken into account: Co and Cu. However, since both atoms are almost indistinguishable as backscatters because their electric scattering characteristics are very similar, we have performed the analysis as if only Co atoms surrounded the absorber. Moreover, although the stable crystalline phase of the Co below $\approx 400 \text{ }^\circ\text{C}$ is hcp, in the present samples crystallizes in fcc structure, as qualitatively deduced from the sole comparison of the Co K -edge x-ray absorption near edge structure (XANES) spectra of all the CoCu samples with a pure fcc Co K -edge spectrum and a hcp Co K -edge one, as displayed in Fig. 5 for $x=15$ sample.

The fitting of the EXAFS signals has been performed in two different ways that have given the same results. The difference between both procedures is the way the backscattering parameters $f(k, \pi)$, and $\phi(k, \pi)$ have been ob-

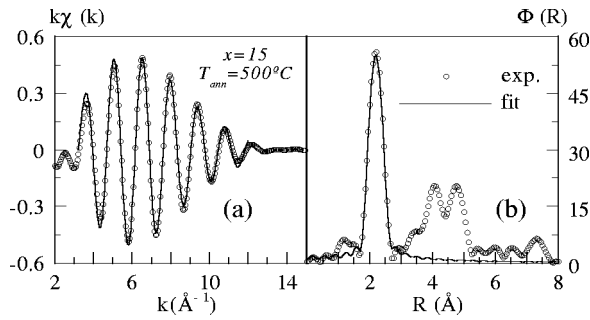


FIG. 6. Fourier filtered EXAFS function and fit in (a) k space and (b) R space, for the sample $\text{Co}_{15}\text{Cu}_{85}$ annealed at 500°C .

tained: first, from an experimental EXAFS spectrum of a pure fcc Co sample collected at 77 K, and second, they have been theoretically generated with the FEFF6.0 codes.³²

The best advantage of the first method is that it reduces the number of fitting parameters, because S_0^2 and Γ are automatically included in the experimental amplitude function. This improves the best fit quality and the reliability of the results. We have isolated the contribution of the nearest neighbors corresponding to the first peak of the Fourier transform ($1.7 < R < 3$ Å) by using the standard Fourier filtering technique and then fitted the filtered data to equation 11 with $j=1$. The error bar in each parameter (± 0.005 Å for the interatomic distance R and 10% for the Debye-Waller factor σ^2) is obtained using the MINOS command of MINUIT,³³ taking into account the effects of correlations between the parameters. In Fig. 6 is displayed the fitting of one of the samples in k and R spaces.

On the other hand, when using theoretically calculated backscattering parameters we have also limited the fitting range to the nearest neighbors in the Fourier transform but have used multiple scattering theory³⁴ for taking into account the contribution of the neighbors up to 5 Å far from the central atom to the first peak of the Fourier transform. In this case the fitting was performed in the R space with the FEFFIT program,³⁵ and the errors were calculated by the fitting program itself.

No discrepancy between both fitting procedures has been found, so we can be really confident of the presented results. The results of both fittings for the interatomic distances R and the Debye-Waller factors σ^2 are displayed in Fig. 7.

IV. DISCUSSION

First of all, let us remark the different and complementary information that each technique, described in the previous section, gives us about the microstructure of the samples at each stage of the annealing. This is to underline that using all the three techniques is necessary for achieving an exhaustive picture of the microstructure of these complex alloys.

The XRD technique is sensitive to the long-range structural order (some ten nm). In all the samples, it detects a Cu-rich fcc phase. In samples $x=10, 15$, and 20, XRD detects also a fraction of all the Co in the samples ($X_{\text{Co}}\%$) arranged in a Co-rich fcc phase. This Co-rich phase grows with the thermal treatment from 20–30 to 90–100 nm size, a

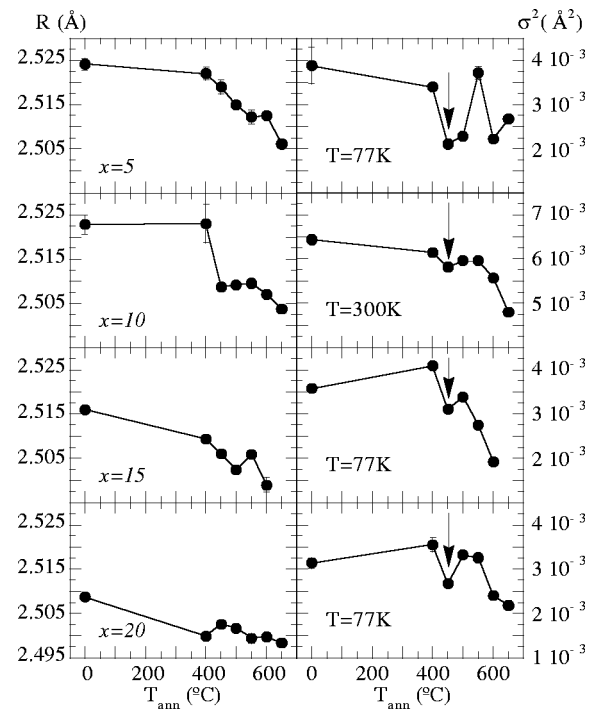


FIG. 7. Evolution of the interatomic distances R and Debye-Waller factors σ^2 with T_{ann} around the Co atoms obtained from the EXAFS analysis using both fitting procedures explained in the text. The difference between both results has been included as an error bar. The arrow marks the point where the GMR is maximum. We also indicate in the figure the measuring temperature of the EXAFS spectra.

grain size which is big enough for presenting a ferromagnetic response. On the other hand, the magnetic analysis performed on the hysteresis loops of the samples distinguishes a ferromagnetic phase, which must be the Co-rich phase previously observed by XRD, and also a superparamagnetic phase composed of Co nanoclusters. The remaining fraction of Co with no magnetic response must be diluted into the Cu matrix. Finally, the EXAFS technique is a short-range order technique and detects all the Co atoms in the sample, no matter which environment they are embedded in. Thus the final results of the EXAFS analysis are an average over all the possible surroundings of the Co atoms in the samples depending on their location, that is, inside the Co-rich ferromagnetic phase, forming the superparamagnetic nanoclusters, diluted into the Cu matrix or at the interfaces. In the following sections we will discuss the results obtained from each technique.

A. XRD

The XRD patterns of $x=5, 10, 15$, and 20 as-quenched and annealed samples display a set of peaks corresponding to a Cu-rich fcc phase of 90–100 nm size. In addition, in the case of the $x=10, 15$, and 20 samples, even at the as-quenched state, the XRD detects a fraction of the Co in the samples ($X_{\text{Co}}\%$, see Table II), arranged in a ferromagnetic fcc phase of 20–30 nm size. Raising the annealing temperature, this Co-rich ferromagnetic phase grows in size up to 90–100 nm

and $X_{\text{Co}}\%$ approaches x , until at $T_{\text{ann}}=650$ °C the majority of the Co atoms are located at this ferromagnetic phase detectable by XRD. Moreover, it is important to note that the evolution of $X_{\text{Co}}\%$ with the annealing temperature is systematic for every x : it remains nearly constant for $T_{\text{ann}} < 550$ °C but increases rapidly from 550 to 650 °C, see Fig. 2(b).

Figures 1 and 2(a) show the evolution of the lattice parameters of the two fcc phases (Cu-rich and Co-rich) as a function of the annealing temperature. For $x=5$, the thermal treatment causes only a slight variation of its unique Cu-rich fcc phase $\Delta a/a \approx 10^{-4}$. The measured lattice parameter ($a \approx 3.614$ Å) is higher than the value estimated from the Vegard's law for a $\text{Co}_5\text{Cu}_{85}$ solid solution ($a \approx 3.611$ Å). This suggests the presence of Co clusters embedded in the Cu-rich phase, not detected by XRD, but expected from the magnetic and magnetotransport results. On the other hand, for both $x=10$ and 20 samples, the thermal treatment causes a different evolution in each phase. The lattice parameter of each phase evolves to the value of pure fcc Cu and pure fcc Co, respectively, as the annealing temperature increases, which is an indication of the segregation process induced by the thermal treatment. In particular, the lattice parameter of the Cu-rich phase exhibits no substantial changes from the as-quenched state to the annealing at $T_{\text{ann}} < 550$ °C, but above this annealing temperature it increases up to the value of the fcc Cu bulk ($a_{\text{fcc Cu}}=3.615$ Å). The global increment of the Cu-rich phase lattice parameter in all the process is $\approx 0.1\%$. On the other hand, the lattice parameter of the Co-rich phase decreases down to the value of the fcc Co bulk ($a_{\text{fcc Co}}=3.544$ Å). In this case, the change of the lattice parameter for the Co-rich phase is larger ($\approx 0.4\%$). The decrease is not monotonous but displays some structure: from the as-quenched state to the annealed at 400 °C the lattice parameter remains unchanged. From 400 to 450 °C it decreases abruptly, evidencing the onset of a demixing process in which the Cu atoms are expelled out of the Co-rich particles. Between 450 and 550 °C the lattice parameter of the Co-rich phase exhibits an anomalous behavior: first, it smooths its decrease and then, between 500 and 550 °C, it increases, suggesting an interruption or even an inversion of the demixing process. Finally, from 550 to 650 °C the segregation process is restarted and the lattice parameter continues its decreasing down to the fcc Co bulk value.

B. Magnetism

The magnetic analysis will give us an indirect view of the microstructure of the samples and it will allow us to follow the evolution with the thermal treatments of the different magnetic phases present in the samples.

The as-quenched samples of each composition present important differences in the distribution of the Co atoms in each magnetic phase, due to the preparation method. As we can see in Table II, in the $x=5$ as-quenched sample, the Co atoms are equally distributed between the SPM phase and diluted into the Cu matrix ($\approx 2.5\%$ in each phase). On the other hand, for both the $x=10$ and 15 as-quenched samples

there is a $\approx 6\%$ of Co in the SPM phase and $\approx 2\%$ in the FM phase, while the amount of diluted Co is 2% for $x=10$ and 7% for $x=15$.

However, we can observe again in Table II that the qualitative evolution with T_{ann} of the percentage of Co in each phase is indeed systematic for the three compositions. Two steps can be readily distinguished in this evolution: up to 500 and above 550 °C.

For $T_{\text{ann}} < 550$ °C, the percentage of Co atoms diluted in the Cu matrix diminishes on behalf of the SPM phase, and the mean diameter in this annealing range of the SPM Co clusters ranges between 2 and 3 nm within the error (see Table III), in agreement with the values found in the bibliography.^{18,36,37} However, there is a slight difference in the $x=15$ as-quenched sample, which presents a very large mean diameter (4.5 Å) that decreases when annealing at 400 °C. This is explained by looking at the evolution of the percentage of FM phase: from the as-quenched state to the annealed at 400 °C it increases abruptly, which means that the big Co nanoclusters present in the as-quenched state have grown with the annealing and crossed the limit of the SPM size, adding to the FM phase at $T_{\text{ann}}=400$ °C. From $T_{\text{ann}}=400$ to 500 °C the percentage of FM phase remains almost unchanged, and this trend is also followed by the $x=10$ even from the as-quenched state.

For $T_{\text{ann}} \geq 550$ °C, in $x=5$ both the SPM phase and the diluted percentage of Co atoms remain almost unchanged and the size of the SPM nanoclusters increases up to 4 nm. In $x=10,15$ samples the SPM phase diminishes on behalf of the FM one, until the latter becomes the unique magnetic contribution at $T_{\text{ann}}=650$ °C. Meanwhile, the mean diameter of the SPM nanoclusters increases rapidly up to 5 nm. It is important to note that in this annealing temperature range (550–650 °C) there is a $\approx 1\%$ of Co atoms that remains diluted into the Cu matrix in $x=5$ as well as in $x=10$ and 15 samples.

Finally, if we compare in Table II the percentage of Co-rich FM phase previously obtained from the XRD analysis ($X_{\text{Co}}\%$) and the data extracted from the magnetic analysis (% FM), we can observe that the evolution of the FM phase with the annealing temperature is coincident in both cases, that is, it remains nearly constant for $T_{\text{ann}} < 550$ °C but increases rapidly from 550 to 650 °C. However, there are some quantitative discrepancies between the data obtained from both techniques due to the limitations of both calculation methods.

In sum, the magnetic analysis gives us an insight into the microstructure of the samples. In fact, it is very important to remark that the magnetic results show that at 500 °C there is still a dominant percentage of SPM phase formed by small magnetic clusters (2–3 nm) likely to produce GMR.

C. EXAFS

EXAFS is a powerful short-range order technique that provides information about the closest neighborhood of the Co atoms. Depending on where the Co atoms are located in the sample, they present different environments: diluted into the Cu matrix, in the Co-rich FM phase with grain sizes

bigger than 20–30 nm, in the 2–4 nm sized SPM nanoclusters or at the interfaces between the nanoclusters and the matrix (for a 2–4 nm size cluster the 60–40% of the atoms are at the interface). In any case, we must remind that the magnetic analysis and also the XRD results show that, for $x=5,10$, and 15 samples at $T_{\text{ann}} < 550$ °C, the majority of the Co is in the SPM phase, thus a large contribution to the EXAFS signal at those stages of the annealing comes from the Co atoms at the SPM nanoclusters.

First, we are going to discuss the evolution of the interatomic distances presented in Fig. 7. The interatomic distance R is the average of the interatomic distances of the Co atoms in the four different environments described above. Each environment presents different values of R and the weight of each environment changes with T_{ann} , thus a correct interpretation of this parameter is extremely difficult. In any case, we can perform a qualitative analysis of its evolution with T_{ann} for every x .

The sample with $x=5$ displays the highest interatomic distances because in this case the Co atoms are diluted into the Cu matrix or forming SPM nanoclusters, thus a great number of Co atoms are surrounded by Cu atoms, and, as the Cu atoms are bigger than the Co ones, the Co-Cu interatomic distance is larger than the Co-Co one. On the contrary, the interatomic distances of the $x=20$ samples are close to that of the fcc Co (2.507 Å) even in the as-quenched state because in this case there is an important percentage of Co atoms in the Co-rich FM phase, thus most of the Co atoms see Co and the interatomic distances are similar to that of the bulk fcc Co. Upon annealing, the interatomic distances of the four compositions studied display an overall decreasing trend down to the value of the fcc Co bulk, which is a clear indication of the segregation of the Co atoms. The decreasing trend of the interatomic distances is not monotonous but presents certain degree of structure in the curves. However, the evolution of the interatomic distances is difficult to interpret because, as mentioned previously, this parameter averages the values of the different environments whose weights change with the thermal treatment and composition.

On the other hand, the interpretation of the Debye-Waller factor σ^2 is easier: it diminishes when the Co atoms reorganize, no matter whether they are in the Co-rich FM phase, in the Co nanoclusters or diluted into the Cu matrix, because σ^2 is a measure of the structural and thermal disorder around the Co atoms. In this case the thermal disorder is the same for all the as-quenched and annealed samples with equal x because they have all been collected at the same temperature, thus the changes of σ^2 with the thermal treatment must come solely from the structural disorder. Evenmore, for $x=5,15$ and 20 the EXAFS spectra were collected at 77 K, thus the contribution of the thermal disorder to the Debye-Waller factor is very small and the most important contribution comes from the chemical disorder. As the atoms at the interfaces between the Co nanoclusters and the matrix present the highest chemical disorder, they constitute the main contribution to σ^2 , at least for $x=5$ and 10, where almost all the Co atoms are forming nanoclusters (2–3 nm) in the SPM phase. For $x=10$, the thermal disorder partly masks the chemical disorder

contribution to σ^2 , since for these samples the EXAFS spectra were collected at room temperature.

The overall decreasing trend of the structural disorder with T_{ann} shown in Fig. 7 is again the fingerprint of a demixing process in which Cu atoms are expelled from the Co local environment and join together towards an ordered fcc Co structure. The decreasing trend of σ^2 is not monotonous, but it displays three stages: from the as-quenched state to $T_{\text{ann}}=450$ °C starts the segregation process of the Co atoms. The annealing between 450 and 500–550°C inverts the initial decreasing trend, pointing out an interruption of the segregation. We attribute this increment of the structural disorder around the Co atoms to a slight redissolution of Co and Cu that starts between 450–500 °C. This effect provokes the interdiffusion of Co and Cu at the interfaces, which constitute the main contribution to the Debye-Waller factor. Thus, it is in the $x=5$ samples where this anomaly in the segregation process is better observed, because in these samples almost all the Co is arranged in nanoclusters (see Table II), and a significant number of Co atoms are at the interfaces. When increasing the annealing temperature, both processes, the redissolution and the segregation, are in competition. For $T_{\text{ann}} \geq 550$ °C, the Debye-Waller factor diminishes again because the FM phase is majority (see Table II) and though the number of atoms at the interfaces decreases and have much less relative contribution to the total structural disorder around the Co atoms (in a 25 nm size cluster only the 6% of Co atoms are at the interface).

D. Correlation between the microstructure and the GMR

The GMR results presented in Table I show that the evolution of the GMR with the thermal treatment is independent of the composition of the samples x : it increases from the as-quenched state to the annealed at 450 °C, where it reaches a maximum, and then it drops at 500 °C and continues decreasing till the end of the thermal treatment. A similar GMR trend with the annealing temperature in the CoCu granular system has been found by other authors.^{18–21}

It is generally accepted that small magnetic particles (high surface-to-volume ratio) highly concentrated [below the percolation threshold $p_c \approx 30\%$ (Ref. 11)] are necessary conditions for an optimum GMR in granular alloys.^{4,11,38,39} The concentration can be given by the distances between neighboring particles, calculated by the following expression for an aleatory arrangement of clusters:⁴⁰

$$t = \left(\frac{6}{\pi N_c} \right)^{1/3} - \bar{D}, \quad (12)$$

where N_c is the number of clusters per unit volume, given by

$$N_c = \frac{\% \text{ SPM}}{100 \left(\frac{\pi}{6} \bar{D}^3 \right)}. \quad (13)$$

These calculi are represented in Fig. 8.

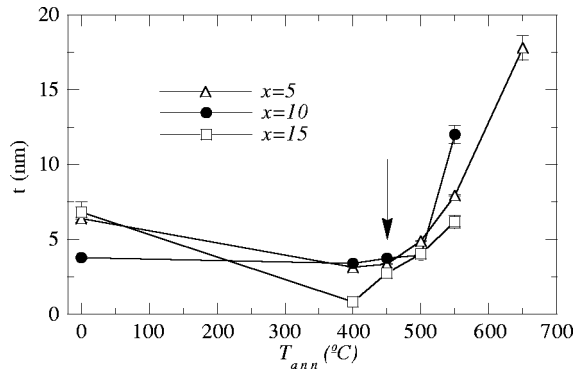


FIG. 8. Mean interparticle distances calculated from Eq. 12 as a function of T_{ann} . The arrow marks the point where the GMR is maximum.

With this in mind, we can summarize the consequences of the thermal treatment on the microstructure of the CoCu granular alloys and its correlation with the GMR response as follows:

(1) Up to 400 °C the annealing induces, on one hand, the precipitation of the Co atoms and thus the creation of SPM nanoclusters from the Co diluted atoms, increasing also the concentration of magnetic nanoparticles (see Table II and Fig. 8). On the other hand, it reduces the interfacial roughness, as deduced from the evolution of the Debye-Waller factor (Fig. 7). These three factors enlarge the GMR, and the $x=15$ sample annealed at 400 °C achieves the maximum value (31%) because it presents the smallest cluster size and also the largest concentration of magnetic particles (minimum t). As long as the thermal treatment goes on (400–450 °C), both the particle size and t increase slightly, but the interfacial roughness decreases slightly (Fig. 7) giving rise to an increase of the GMR in $x=5, 10$ and 20 samples.

(2) Between $450 < T_{ann} < 550$ °C both \bar{D} (Table III) and t (Fig. 8) keep on increasing slightly. Meanwhile, the lattice parameter of the Co-rich FM phase stops its decreasing to the fcc Co bulk value [see Fig. 2(a)] and, at the same time, the Debye-Waller factor detects an enhancement of the structural disorder at the interfaces of the Co clusters (see Fig. 7). We attribute this interruption in the segregation process to a slight solubility of Co and Cu that starts at ≈ 500 °C. In fact, in the CoCu phase diagram⁴¹ it becomes apparent that above ≈ 500 °C the Cu redissolves into the Co. This mechanism induces the interdiffusion of Co and Cu, roughening the interfaces of the Co granules, particularly in the nanometer-sized ones to which is attached the existence of GMR and degrades it abruptly at the same time independently of x because this effect is intrinsic to the CoCu system. A number of theoretical studies about the correlation between the microstructure and the GMR in granular alloys account for the need of rough interfaces between the magnetic and metallic element for enhancing the GMR.^{4,13,12} These theories are all based on previous studies on multilayers, where the chemical disorder at the interfaces of the magnetic-non magnetic layers has been observed to enhance the GMR in many

systems.^{1,42} However, there is experimental evidence of the degrading of the GMR due to interfacial roughness in Co/Cu multilayers by Hall *et al.*⁴³ and Suzuki and Taga,⁴⁴ and this has been also observed in other systems of multilayers such as Co/Ag (Ref. 45) and NiFe/Cu.⁴⁶ Thus, although the theory of the GMR for granulars differs from our experimental results, the findings in Co/Cu multilayers justify our conclusions.

(3) For $T_{ann} \geq 550$ °C, the redissolution of Co and Cu also explains the $\approx 1\%$ of Co that remains diluted into the Cu matrix observed in the magnetic analysis (Table II). Despite the solubility of Co and Cu, the percentage of FM phase ($X_{Co}\%$) increases, decreasing the SPM one [see Figs. 2(b) and Table II], and as a consequence the Co-rich FM phase lattice parameter decreases to the fcc Co bulk one [Fig. 2(a)] and also the Debye-Waller factor diminishes (Fig. 7). This means that the magnetic clusters surface-to-volume ratio decreases rapidly, decreasing the influence of the interfacial roughness in the GMR response and also the nanoclusters concentration, which degrades the GMR, that diminishes to zero.

This way, our microstructural study on the CoCu granular alloys has provided experimental evidence of the direct correlation between the GMR and the microstructural properties of the samples. In particular, we have demonstrated that the interfacial roughness plays a significant role in the GMR response of the CoCu granular alloys, and even regulates the GMR changes when both the magnetic particles sizes and distances among them are small, enhancing the GMR as the interfacial roughness decreases.

V. CONCLUSIONS

We have studied the changes induced by the thermal treatment in the microstructure of the Co_xCu_{100-x} ($x=5, 10, 15, 20$) melt-spun granular alloys and related them to the changes in the GMR. The as-quenched samples contain a majority of Co SPM nanoclusters responsible of the GMR phenomenon coexisting with a percentage of Co atoms diluted into the Cu matrix and, in $x=10, 15$, and 20 samples, also with a Co-rich FM phase. The thermal treatment induces the segregation of the Co atoms from the Cu matrix, changing the percentage of each magnetic phase: for $T_{ann} < 550$ °C the diluted percentage diminishes on behalf of the SPM phase while the FM percentage remains unchanged, and for $T_{ann} \geq 550$ °C the FM phase suddenly increases on behalf of the SPM one and there is a $\approx 1\%$ of Co atoms diluted into the Cu matrix. This deep knowledge of the microstructure at each stage of the annealing has allowed us to experimentally demonstrate the main factors that lead to the optimum GMR response in CoCu granular alloys: large surface-to-volume ratio and concentration of the magnetic clusters and smooth interfaces.

ACKNOWLEDGMENTS

This work has been supported by the spanish CICyT under Project No. MAT02-04178. A.G.P. thanks the University of the Basque Country for financial support.

- *Email address: agp@we.lc.ehu.es
- ¹M.N. Baibich, J.M. Broto, A. Fert, F. Nguyen Van Dau, F. Petroff, P. Etienne, G. Creuzet, A. Friederich, and J. Chazeles, *Phys. Rev. Lett.* **61**, 2472 (1988).
 - ²A.E. Berkowitz, J.R. Mitchell, M.J. Carey, A.P. Young, S. Zhang, F.E. Spada, F.T. Parker, A. Hutten, and G. Thomas, *Phys. Rev. Lett.* **68**, 3745 (1992).
 - ³J.Q. Xiao, J.S. Jiang, and C.L. Chien, *Phys. Rev. Lett.* **68**, 3749 (1992).
 - ⁴S. Zhang and P.M. Levy, *J. Appl. Phys.* **73**, 5315 (1993).
 - ⁵T.A. Rabedeau, M.F. Toney, R.F. Marks, S.S.P. Parkin, R.F.C. Farrow, and G.R. Harp, *Phys. Rev. B* **48**, 16 810 (1993).
 - ⁶Y. Asano, A. Oguri, J. Inoue, and S. Maekawa, *Phys. Rev. B* **49**, 12 831 (1994).
 - ⁷R.Y. Gu, L. Sheng, D.Y. Xing, Z.D. Wang, and J.M. Dong, *Phys. Rev. B* **53**, 11 685 (1996).
 - ⁸R. Yang, W. Zhang, and W.J. Shong, *J. Appl. Phys.* **84**, 2044 (1998).
 - ⁹M. Rubinstein, *Phys. Rev. B* **50**, 3830 (1994).
 - ¹⁰Xiao Chuanyun, Yang Jinglong, Deng Kaiming, and Wang Kelin, *Phys. Rev. B* **55**, 3677 (1997).
 - ¹¹D. Kechrakos and K.N. Trohidou, *Phys. Rev. B* **62**, 3941 (2000).
 - ¹²R. Yang and W.J. Song, *Phys. Status Solidi B* **206**, 797 (1998).
 - ¹³E.F. Ferrari, F.C.S. da Silva, and M. Knobel, *Phys. Rev. B* **56**, 6086 (1997).
 - ¹⁴M.L. Fdez-Gubieda, A. García Prieto, A. García-Arribas, C. Meneghini, and S. Mobilio, *Europhys. Lett.* **59**, 855 (2002).
 - ¹⁵*Binary Alloy Phase Diagrams*, edited by T.B. Massalsky *et al.* (ASM International, Ohio, 1987), Vol. 1, pp. 16, 760, 25, 942.
 - ¹⁶J.Q. Wang and G. Xiao, *Phys. Rev. B* **49**, 3982 (1994).
 - ¹⁷J.C. Soares, L.M. Redondo, C.M. de Jesús, J.G. Marques, M.F. da Silva, M.M. Pereira de Acevedo, J.A. Mendes, S. Rogalski, and J.B. Sousa, *J. Vac. Sci. Technol. A* **16**, 1812 (1998).
 - ¹⁸A.D.C. Viegas, J. Geshev, L.S. Dornless, J.E. Schmidt, and M. Knobel, *J. Appl. Phys.* **82**, 3047 (1997).
 - ¹⁹J. Wecker, R. von Helmolt, L. Schultz, and K. Samwer, *IEEE Trans. Magn.* **29**, 3087 (1993).
 - ²⁰B. Dieny, A. Chamberod, J.B. Genin, B. Rodmacq, S.R. Teixeira, S. Auffret, P. Gerard, O. Redon, J. Pierre, R. Ferrer, and B. Barbara, *J. Magn. Mater.* **126**, 433 (1993).
 - ²¹R.H. Yu, X.X. Zhang, J. Tejada, J. Zhu, and M. Knobel, *J. Appl. Phys.* **79**, 1979 (1996).
 - ²²C. Meneghini, G. Artioli, P. Norby, A. Balerna, A. Gualtieri, and S. Mobilio, *J. Synchrotron Radiat.* **8**, 1162 (2001).
 - ²³A.C. Larson and R.B. von Dreele (unpublished).
 - ²⁴F.E. Luborsky, *J. Appl. Phys.* **32**, 171S (1961).
 - ²⁵B.D. Cullity, *Introduction to Magnetic Materials* (Addison-Wesley, New York, 1972), p. 411.
 - ²⁶L. Råde and B. Westergren, *Mathematics Handbook for Science and Engineering* (Studentlitteratur, 1995), p. 432.
 - ²⁷P. Allia, M. Coisson, M. Knobel, P. Tiberto, and F. Vinai, *Phys. Rev. B* **60**, 12 207 (1999).
 - ²⁸M. B. Stearns and Y. Cheng, *J. Appl. Phys.* **75**, 6894 (1994).
 - ²⁹PRO FIT 5.5, by QuantumSoft, <http://www.quansoft.com/>
 - ³⁰B. Lengeler and P. Eisenberger, *Phys. Rev. B* **21**, 4507 (1980).
 - ³¹E. A. Stern, *Contemp. Phys.* **18**, 289 (1978).
 - ³²S. I. Zabinsky, J.J. Rehr, A. Ankudinov, R.C. Albers, and M.J. Eller, *Phys. Rev. B* **52**, 2995 (1995).
 - ³³F. James (unpublished).
 - ³⁴E.A. Stern, in *X-ray Absorption: Principles, Applications, Techniques of EXAFS, SEXAFS and XANES*, edited by D.C. Koningsberger and R. Prins (Wiley, New York), p. 45.
 - ³⁵E.A. Stern, M. Newville, B. Ravel, Y. Yacoby, and D. Haskel, *Physica B* **208&209**, 117 (1995).
 - ³⁶P. Allia, M. Knobel, P. Tiberto, and F. Vinai, *Phys. Rev. B* **52**, 15 398 (1995).
 - ³⁷B.R. Pujada, E.H.C.P. Sinnecker, A.M. Rossi, and A.P. Guimarães, *Phys. Rev. B* **64**, 184419 (2001).
 - ³⁸S. Rubin, M. Holdenried, and H. Micklitz, *Eur. Phys. J. B* **5**, 23 (1998).
 - ³⁹P. Allia, M. Coisson, P. Tiberto, F. Vinai, M. Knobel, M.A. Novak, and W.C. Nunes, *Phys. Rev. B* **64**, 144420 (2001).
 - ⁴⁰S. Honda, M. Nawate, M. Tanaka, and T. Okada, *J. Appl. Phys.* **82**, 764 (1997).
 - ⁴¹T. Nishizawa and K. Ishidam, *Bull. Alloy Phase Diagrams* **5**, 161 (1984).
 - ⁴²E.E. Fullerton, D.M. Kelly, J. Guimpel, I.K. Schuller, and Y. Bruynseraede, *Phys. Rev. Lett.* **68**, 859 (1992).
 - ⁴³M.J. Hall, B.J. Hickey, M.A. Howson, M.J. Walker, J. Xu, D. Greig, and N. Wiser, *Phys. Rev. B* **47**, 12 785 (1993).
 - ⁴⁴M. Suzuki and Y. Taga, *Phys. Rev. B* **52**, 361 (1995).
 - ⁴⁵Wen-C. Chiang, W.P. Pratt, M. Herrold, and D.V. Baxter, *Phys. Rev. B* **58**, 5602 (1998).
 - ⁴⁶V.S. Speriosu, J.P. Nozieres, B.A. Gurney, B. Dieny, T.C. Huang, and H. Lefakis, *Phys. Rev. B* **47**, 11 579 (1993).